Journal of Power Sources 204 (2012) 46–52

Contents lists available at SciVerse ScienceDirect

Journal of Power Sources

journal homepage: www.elsevier.com/locate/jpowsour

Graphene nanoplate-Pt composite as a high performance electrocatalyst for direct methanol fuel cells

Huajie Huang[a], Haiqun Chen[b], Dongping Sun[a], Xin Wang[a,*]

[a] Key Laboratory of Soft Chemistry and Functional Materials (Nanjing University of Science and Technology), Ministry of Education, Nanjing 210094, China
[b] Key Laboratory of Fine Petrochemical Engineering, Changzhou University, Changzhou 213164, China

ARTICLE INFO

Article history:
Received 14 October 2011
Received in revised form 6 December 2011
Accepted 1 January 2012
Available online 9 January 2012

Keywords:
Graphene nanoplate
Pt nanoparticles
Electrocatalyst
Direct methanol fuel cells

ABSTRACT

A soft chemical method has been developed to load Pt nanoparticles on graphene nanoplates (GNPs) without damaging their graphene structures. Our approach does not require cumbersome oxidation of graphite in advance and needs no subsequent reduction of graphene oxide (GO) with reducing agents or by thermal treatment. Transmission electron microscope observation reveals that Pt nanoparticles with an average diameter of 2.3 nm are uniformly dispersed on the GNP surface. Raman spectroscopy confirms the GNPs have a very low defect density. This graphene nanoplate-Pt (GNP/Pt) composite exhibits superior electrochemical activity and high poison tolerance toward methanol oxidation compared to reduced graphene oxide-Pt (RGO/Pt) and Vulcan XC-72-Pt (XC-72/Pt) with the same Pt content, which demonstrate that the GNPs can be used as promising electrocatalyst supports for direct methanol fuel cells.

1. Introduction

In the past few decades, great efforts have been devoted to the design and development of fuel cells as new power sources because of the depletion of fossil fuels and the increasing concerns of environmental issues [1–3]. As an ideal power source for portable electronics, direct methanol fuel cells (DMFC) have attracted considerable and persistent attention owing to their high-energy conversion efficiency, low pollutant emission and low operating temperature [4–6]. However, challenging issues such as methanol crossover, poor methanol electrooxidation kinetics and the adverse effects of intermediate species, are the critical obstacles inhibiting broad applications of DMFC [7,8].

A promising strategy to overcome the above problems is development of a novel class of electrocatalysts with higher poison tolerance and greater methanol oxidation activity. It is well-known that the most widely used catalysts in DMFC systems are Pt-based nanocomposites, in which Pt nanoparticles are incorporated into carbon support materials, such as carbon black (CB) [9–11], graphite nanofibers (GNFs) [12–14] and carbon nanotubes (CNTs) [15–20]. Recently, graphene as catalyst support has incurred intense interest in fuel cell applications due to its unique, outstanding physicochemical properties, such as extremely high specific surface area (2600 $m^2 g^{-1}$), superior electronic conductivity, large surface to volume ratio and high stability [21–24]. The combination of Pt nanoparticles and 2D-structure graphene opens up new possibilities for designing the next generation catalysts [25,26]. Additionally, the Pt particles supported on the graphene seem to be less susceptible to CO poisoning than those deposited onto traditional carbon supports [27,28].

A few methods have been adopted to attach Pt nanoparticles onto the surface of graphene [29–32]. In these methods, graphene oxide (GO) sheets are generally used as the raw materials or precursors of graphene sheets because of their good dispersibility in water and some organic solvents [27–32]. As shown in Scheme 1, graphite oxide is produced by the oxidative treatment of graphite. The graphene-derived sheets in graphite oxide are bearing hydroxyl and epoxide functional groups on their basal planes, in addition to carbonyl and carboxyl groups located at the sheet edges [33]. These oxygen functionalities can stabilize the dispersion of the GO sheets in water and play a role for anchoring Pt nanoparticles onto the graphene sheets [25]. However, such surface functionalization may destroy the intrinsic structure of graphene because of the transformation of carbon atoms from a planar sp^2-hybridized geometry to a distorted sp^3-hybridized geometry [33,34]. Although the functional groups can be removed by chemical or thermal reduction, it is inevitable that a significant amount of framework defects will be produced during the deoxygenation process. The electrical and mechanical properties of the reduced GO are severely impaired by the defects and the purity of the composite is decreased due to the fragments [35,36]. In addition, it is verified that these defects can make the graphene-based catalysts less stable under harsh electrochemical conditions because the corrosion of carbon materials always initiates at the defect sites [37,38]. Moreover, in such a laborious and costly oxidation–reduction process, some environmental incompatible agents are widely used. Therefore, a

* Corresponding author. Tel.: +86 25 84305667; fax: +86 25 84315054.
E-mail address: wxin@public1.ptt.js.cn (X. Wang).

0378-7753/$ – see front matter © 2012 Elsevier B.V. All rights reserved.
doi:10.1016/j.jpowsour.2012.01.023

more mild and straightforward method is highly desired to avoid introducing excessive defects to the graphene sheets.

In a recent study, we developed an in situ oxidation route to directly fabricate graphene nanoplate–metal oxide (Ag_2O, Co_3O_4, Cu_2O and ZnO) and multiwalled carbon nanotube (MWNT)-Pt composites [15,39]. For the latter, this mild and straightforward route can effectively avoid excessive interruption of the basic structure and the as-obtained catalyst shows good catalytic performance on electrooxidation of methanol.

Here, the similar method was applied for the synthesis of graphene nanoplate-Pt (GNP/Pt) composites by in situ oxidation of graphene nanoplates (GNPs). As shown in Scheme 1, GNPs can be obtained from dispersion and exfoliation of bulk graphite in NMP mainly due to the fact that the energy required to exfoliate graphene can be balanced by the solvent–graphene interaction [34]. We utilize H^+ from hydrolysis of platinum nitrate in combination with NO_3^- to introduce oxygen-containing groups onto the graphene sheets, then the in situ formation of Pt nanoparticles on the carbon sheets takes place. In the above process, only a very small number of structural defects in GNP formed because of the concentration of H^+ produced from hydrolysis was much lower compared with that of traditional oxygenation processes (where strong oxidation reagents, such as sulfuric acid, nitric acid, etc., were used) [39]. The relatively intact crystal structure of graphene in the composite leads to a very low charge transfer resistance and an excellent electrochemical performance.

2. Experimental

2.1. Materials

Natural flake graphite with an average particle size of 40 μm was purchased from Qingdao Zhongtian Company (Qingdao, China). Vulcan XC-72 was purchased from Cabot Corp. $Pt(NO_3)_2$ solution was obtained from Shanghai July Chemical Co. Ltd. (Shanghai, China). K_2PtCl_4 was purchased from Alfa Aesar. Nafion 117 was purchased from Dupont. All other chemicals employed were of analytical grade and used as received. All aqueous solutions were prepared using deionized water.

2.2. Synthesis of graphene nanoplate-Pt, reduced graphene oxide-Pt and Vulcan XC-72-Pt composites

GNPs were produced by dispersion and exfoliation of bulk graphite in NMP at a starting concentration of 0.1 mg mL^{-1} according to Colman et al. [34]. In a typical synthesis route, ethylene glycol (30 mL) and 0.017 mL of 0.45 M $Pt(NO_3)_2$ solution were added to 50 mL of the as-obtained GNPs dispersion with magnetic stirring for 15 min. The resulting suspension was transferred into a 100 mL Teflon-lined stainless steel autoclave and sealed tightly. The autoclave was then heated to 120 °C and kept there for 12 h. After the solvothermal treatment, the nanocomposite, denoted as GNP/Pt, was centrifuged, washed, and finally dried in air at 60 °C overnight. For comparison, GO was prepared from powdered flake graphite by a modified Hummers method as described previously [40]. According to the previous reports [25,27], the typical route to prepare reduced graphene oxide-Pt nanocomposite is as follows: GO (5 mg) were dispersed in 80 mL of ethylene glycol and sonicated for 1 h. Then 7.65 mL of 0.01 M K_2PtCl_4 (or 0.17 mL of 0.45 M $Pt(NO_3)_2$)was introduced to the solution with magnetic stirring for 15 min. Subsequently, similar solvothermal treatment was used and the composite was denoted as RGO/Pt. Pt supported on Vulcan XC-72 was prepared by the same procedure and the composite was denoted as XC-72/Pt.

2.3. Characterization

Powder X-ray diffraction (XRD) analyzes were performed on a Bruker D8 Advance diffractometer with Cu Kα radiation ($\lambda \approx 1.54$ Å). Raman spectra of all the samples were collected using a Renishaw Raman microscope. X-ray photoelectron spectra (XPS) were recorded on a RBD upgraded PHI-5000C ESCA system (Perkin Elmer) with Al Kα radiation ($h\nu = 1486.6$ eV). Ultraviolet–visible (UV–vis) absorption spectra were collected using a BRAIC UV-1201 spectrophotometer. Transmission electron microscopy (TEM) measurements were performed on a JEOL JEM-2100 microscope operating at 200 kV, by depositing a drop of sample dispersion onto 300 mesh Cu grids coated with a carbon layer. AFM images were obtained with an Autoprobe CP 5 Research System (Veeco Instruments). Samples for AFM imaging were prepared by drop-casting the dispersions onto freshly cleaved mica substrates, which were then allowed to dry in air.

2.4. Electrochemical activity measurement

Electrocatalytic activities of samples were measured in a conventional three electrode cell using a CHI 660B electrochemical workstation. The three-electrode cell consisted of a Pt wire serving as the counter electrode, a saturated calomel electrode (SCE) serving as the reference electrode and a glassy carbon (GC) disk (3 mm in diameter) with coated catalysts serving as the working electrode. The work electrode was manufactured as follows: 2 mg of catalyst powder was dispersed in a mixed solution (500 μL of water,

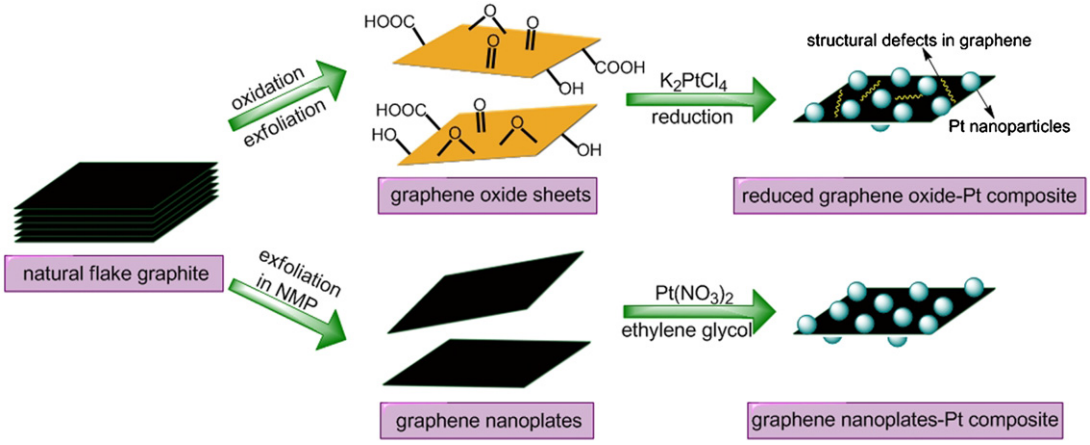

Scheme 1. Illustrations of the synthesis of reduced graphene oxide-Pt composite and graphene nanoplate-Pt composite by traditional oxidation–reduction method and our soft chemical method, respectively.

500 μL of ethanol and 50 μL of 5% Nafion 117 solution) with ultrasonication for 30 min to form a homogeneous black suspension. Then 20 μL of the resulting suspension was carefully pipetted onto the GC electrode surface, and the coating was dried at room temperature for 1 h. The ECSA values of the catalysts were determined by cyclic voltammetry (CV) of the hydrogen absorption/desorption in 1 M H_2SO_4 solution at room temperature. The electrocatalytic activity of the as-prepared catalysts for the methanol oxidation was characterized by collecting CVs in a N_2-purged 1 M H_2SO_4 and 2 M methanol solution at a scan rate of 20 mV s^{-1}. Several activation scans were performed until reproducible voltammograms were obtained. Only the last voltammograms were used for comparing the catalytic activity of the specified catalysts. The chronoamperometry tests were conducted at 0.5 V for a period of 30 min. The chronopotentiometric curves were recorded in 1 M H_2SO_4 and 2 M methanol solution. The value of the applied current was obtained at 0.5 V from the forward scan of the corresponding cyclic voltammogram. Electrochemical impedance spectra (EIS) were recorded at frequencies from 10^5 to 0.02 Hz in a solution of 2 M methanol and 1 M H_2SO_4, and the amplitude of modulation potential was 10 mV.

3. Results and discussion

Fig. 1 shows typical X-ray diffraction (XRD) patterns of the as-prepared GNP/Pt (curve 1) and RGO/Pt (curve 2) composites. For GNP/Pt, the broad peak at around $2\theta = 25.0^\circ$ can be indexed to the (0 0 2) reflection of GNPs, implying the composite contained few-layer graphene sheets. In curve 2, the suppression of the GO peak indicates that the conjugated graphene network (sp^2 carbon) has been reestablished due to the reduction process [29]. Meanwhile, the diffraction peaks observed at 39.5°, 46.8° and 67.6° correspond to the (1 1 1), (2 0 0) and (2 2 0) planes of the face-centered cubic (fcc) structure of Pt, respectively (JCPDS 87-0646). Our results correlate well with the previous studies [27,29], suggesting the RGO/Pt composite was successfully prepared by the solvothermal method. In addition, it was found the absolute intensity of the Pt characteristic peaks was higher for RGO/Pt than GNP/Pt, indicating higher crystallinity of Pt deposited on the RGO support. This is mainly due to the fact that the oxygen-containing groups on GO were much more numerous than those on GNPs, which can facilitate the formation of crystalline Pt onto the RGO surface. The (2 2 0) peak can be used to calculate the average Pt particle size of according to the Scherrer equation [41]:

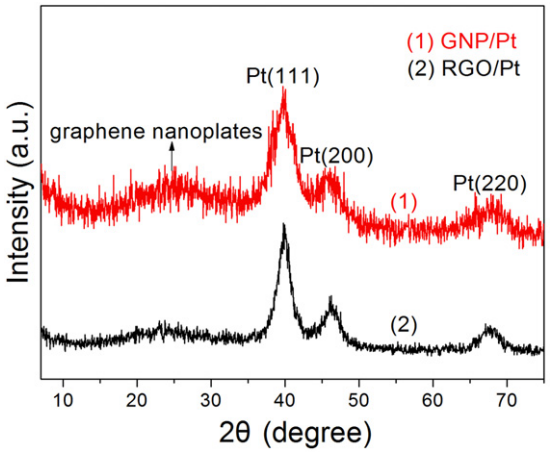

Fig. 1. XRD patterns of GNP/Pt and RGO/Pt.

$$d = \frac{0.9\lambda}{\beta_{1/2}\ \cos\theta} \quad (1)$$

where d is the average particle size (nm), λ is the wavelength of the X-ray used (0.15406 nm), $\beta_{1/2}$ is the width of the diffraction peak at half height in radians and θ is the angle at the position of the peak maximum. The calculated average particle sizes of Pt supported on GNPs and RGO are 2.2 nm and 3.8 nm, respectively. The better dispersion of Pt nanoparticles on GNPs can be attributed to the much softer synthetic conditions of GNP/Pt, which introduce an adequate, but not excessive, amount of functional groups on GNPs. As for RGO/Pt, although plenty of oxygen-containing groups on GO can promote the deposition of Pt particles, the rough RGO surface and the random distribution of excessive groups resulted in the uneven dispersion of Pt nanoparticles.

The sizes and morphologies of Pt nanoparticles deposited on GNPs and RGO have been studied by TEM. As shown in Fig. 2a, the almost transparent carbon sheets suggested that natural flake graphite could be successfully exfoliated into graphene nanoplates by ultrasonic treatment in NMP. Moreover, it is clearly seen that the nanoscale Pt metal particles with diameters ranging from 1 to 5 nm were well-dispersed on the GNP support material though no pretreatment steps were used. The d-spacing value of 0.22 nm coincides with that of face centered cubic (fcc) Pt (1 1 1) [30]. However, in the case of the RGO support, it can be seen that the Pt nanoparticles easily form aggregates, as pointed out by the circles in Fig. 2c. This is probably caused by the uneven distribution of the functional groups on the GO surface. Fig. 2b and d display the size distribution of the Pt nanoparticles on GNP and RGO supports obtained by measuring the sizes of 100 randomly chosen particles in the magnified TEM images. It was found that the average diameters of Pt nanoparticles were about 2.3 nm and 3.7 nm for GNP/Pt and RGO/Pt, respectively, consistenting with the results based on Scherrer equation. High dispersion of Pt nanoparticles on carbon supports is essential to the electrocatalytic activity of the composites for methanol oxidation, which will be described below.

X-ray photoelectron spectroscopy (XPS) is a powerful technique to characterize the elemental and chemical composition of materials. Fig. 3 presents the C 1s and Pt 4f XPS spectra of RGO/Pt and GNP/Pt hybrids. As displayed in Fig. 3a and b, the peak fitting of the C 1s band yielded four components, which centered at 284.6 eV, 286.3 eV, 287.8 eV and 289.0 eV corresponding to the sp^2-hybridized C—C, C—OH, C—O—C and HO—C=O groups, respectively [7]. The prominent sp^2-hybridized C—C peaks indicate a dominant graphitic structure for both samples. The relatively weaker intensities of oxygen-containing groups in GNP/Pt confirmed that the contents of oxygen moieties were significantly lower in GNP/Pt than in RGO/Pt, which can be attributed to the much softer synthetic conditions of GNP/Pt. The content of oxygen moieties in GNP/Pt was further investigated using UV–vis spectroscopy. As shown in Fig. S1, the spectrum obtained for GO exhibits a maximum at 230 nm (attributed to $\pi \rightarrow \pi^*$ transitions of aromatic C—C bonds) and a shoulder at 300 nm (ascribed to $n \rightarrow \pi^*$ transitions of C=O bonds). In the case of GNP/Pt, the spectrum is characteristic of a broad transition band centered at 273 nm (ascribed to $\pi \rightarrow \pi^*$ transitions of electrons in graphene associated with plasmon resonance), suggesting the oxygen-containing groups in GNP/Pt existed in small quantities [23]. In Fig. 3c and d, the Pt 4f spectral features of RGO/Pt and GNP/Pt are similar. It can be seen that the Pt 4f signal is composed of two pairs of doublets: the most intense doublet (71.4 and 74.7 eV) is due to metallic Pt; the second doublet (72.0 and 76.0 eV) can be assigned to the +2 oxidation state of Pt. These values are in good agreement with previous reports [42–44]. The XRD and XPS results imply that GNPs and crystalline Pt coexist in the as-synthesized hybrid.

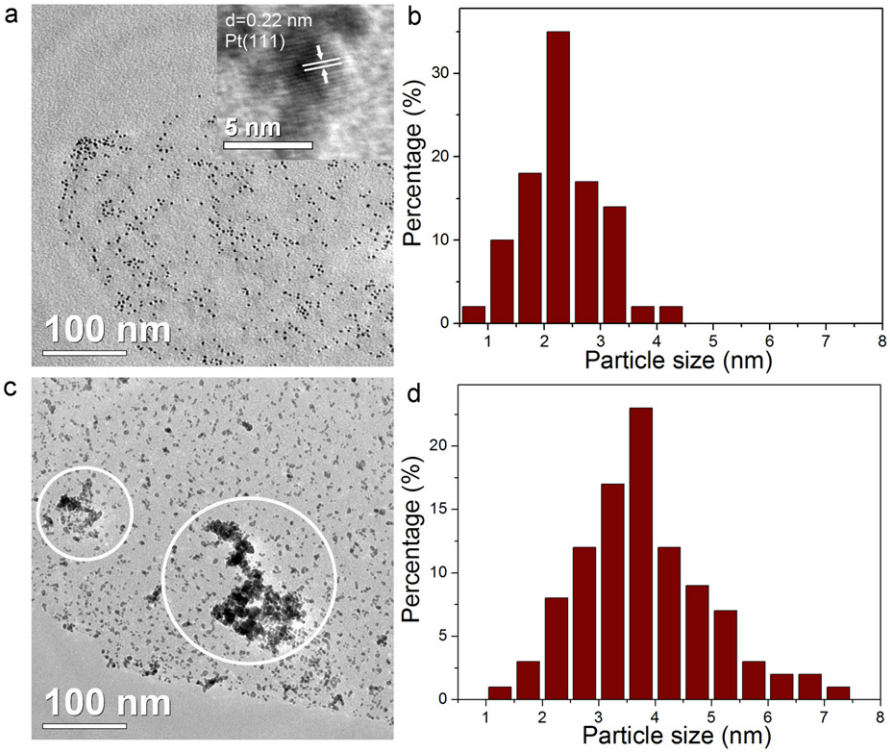

Fig. 2. TEM images and histograms of Pt particle size distribution of (a and b) GNP/Pt and (c and d) RGO/Pt. The inset of (a) is an HETEM image of GNP/Pt.

Fig. 4a shows a typical AFM image of GNP/Pt with the corresponding height profiles. It is found that the sample exhibits a layered structure with lateral dimensions of several micrometers, demonstrating the individual GNP remain isolated after being modified with metal particles. The section analysis of the image indicates a background height of 1.0–1.5 nm which corresponds to the GNP thickness. This value is remarkably higher than that of pristine graphene (0.34 nm). In addition, the height of a typical Pt particle anchored on GNP surface was measured to be ~2.5 nm, which was very close to the aforementioned XRD and TEM results. AFM analysis further confirms our ability to achieve uniform distribution of Pt nanoparticles on micron scale GNPs.

Raman spectroscopy has been widely used for characterizing carbon materials, specifically for analyzing the structure and the

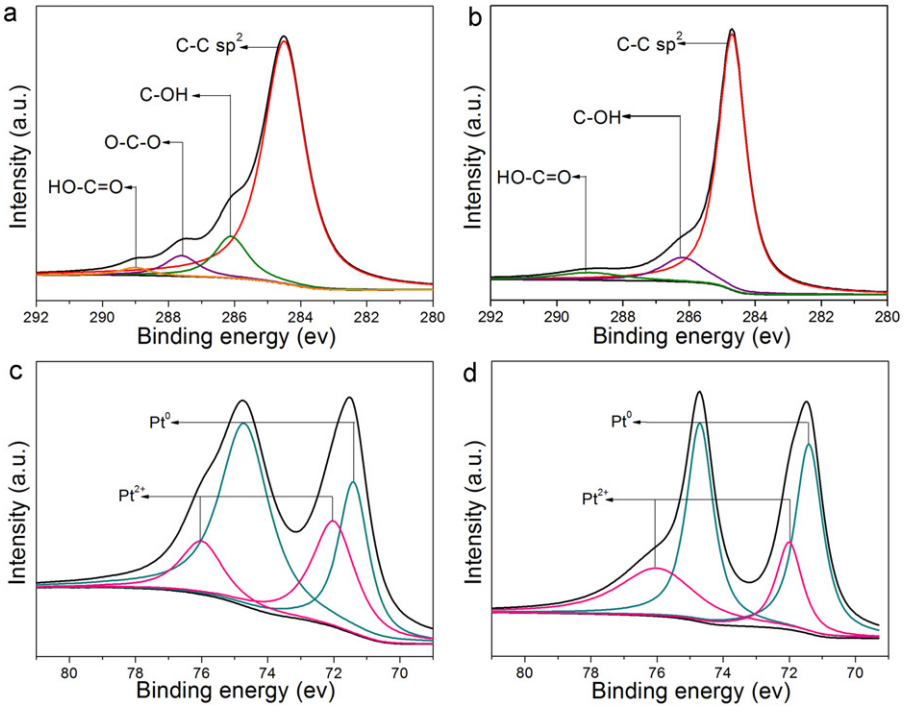

Fig. 3. C 1s core-level XPS spectra of (a) RGO/Pt and (b) GNP/Pt; Pt 4f core-level XPS spectra of (c) RGO/Pt and (d) GNP/Pt.

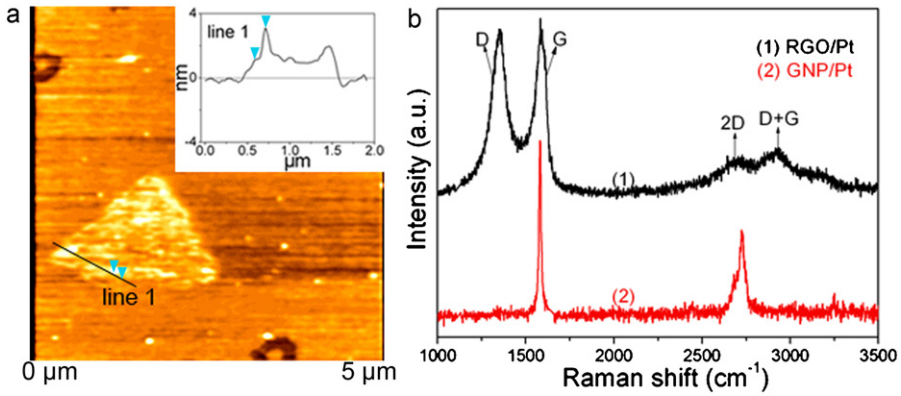

Fig. 4. (a) AFM image (5 μm × 5 μm) and the cross-sectional analysis of GNP/Pt. (b) Raman spectra of RGO/Pt and GNP/Pt.

ratio of sp^2/sp^3 carbon atoms. As shown in Fig. 4b, RGO/Pt composite (spectrum 1) synthesized by traditional oxygenation route exhibits two distinct bands appearing at around 1350 cm^{-1} (defect-induced D-band) and 1570 cm^{-1} (tangential G-band) [45]. The high intensity of D-band implies that there are a large number of structural defects in the graphene composite, and once formed, these defects can be difficult to eliminate even using reducing reagents. On the contrary, it can be seen from spectrum 2 that the D-band is invisible in the Raman spectrum of GNP/Pt, indicating that the sample has a very low density of lattice defects in graphene. This provides evidence that the highly ordered structure of pristine graphene was preserved almost perfectly in the soft chemical process. It is noteworthy that there are additional peaks of overtone (2D) and combination bands (D + G) induced by local defects and disorder in sp^2 phase in the Raman spectrum of RGO/Pt [46]. The peak position (2690 cm^{-1}) of the 2D band is similar to that of a mono-layer graphene [47,48]. In combination with the XRD results, it can be seen that a remarkably small amount of multi-layer carbon sheets is present in RGO/Pt. However, there is only a 2D band appearing at around 2725 cm^{-1} in GNP/Pt, indicating the composite possesses the graphene multiple-layer structure [47,48].

The electrochemically active surface area (ECSA) provides important information regarding the number of electrochemically active sites per gram of catalyst. The CV measurements on XC-72/Pt, RGO/Pt and GNP/Pt were performed in a N_2-saturated solution of 1 M H_2SO_4 at a potential scan rate of 20 mV s^{-1}, and the results are presented in Fig. 5a. ECSA values can be calculated from the coulombic charge for the hydrogen adsorption and desorption (Q_H) in the negative-going potential scan (0 to −0.2 V vs SCE) according to the following formula [49]:

$$\mathrm{ECSA} = \frac{Q_H}{[\mathrm{Pt}] \times 0.21} \quad (2)$$

where [Pt] represents the platinum loading (g cm^{-2}) in the electrode, Q_H is the charge for hydrogen desorption (mC cm^{-2}), and 0.21 represents the charge required to oxidize a monolayer of H_2 on bright Pt (mC cm^{-2}). The calculated results show that GNP/Pt exhibits a higher ECSA value (63.0 m^2 g^{-1}) than RGO/Pt (53.6 m^2 g^{-1}) (Table 1), clearly demonstrating that GNP/Pt possesses a relatively high electrochemical activity compared to RGO/Pt. Moreover, when Vulcan XC-72 served as a supporting material, the ECSA value of the catalyst was only 33.7 m^2 g^{-1}, much less competitive than that of GNPs. These phenomena resulted from the high dispersion of Pt nanoparticles on the 2D carbon material and the preserved electrical conductivity in GNP/Pt because of the low defect density of GNPs.

Table 1
Compiled study comparing CV results for different carbon-based samples [27,32,51].

Electrode	ECSA (m^2 g^{-1})	I_F (mA cm^{-2})	I_R (mA cm^{-2})	I_F/I_R ratio
GNP/Pt	63.0	57.7	47.5	1.21
RGO/Pt	53.6	44.2	52.1	0.85
XC-72/Pt	33.7	17.5	15.1	0.86

Pt nanoparticles supported on Vulcan XC-72, reduced graphene oxide and graphene nanoplates were tested for methanol oxidation reaction in acid medium using cyclic voltammetry. The resulting cyclic voltammograms are shown in Fig. 5b and the relevant data are listed in Table 1. All CV curves show a similar methanol oxidation current peak in the forward scan and an oxidation peak of

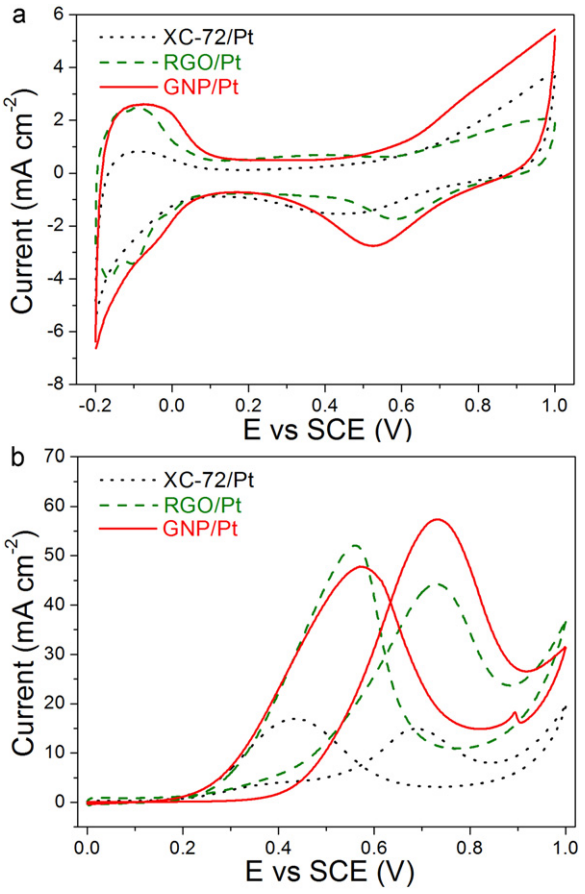

Fig. 5. (a) CVs of XC-72/Pt, RGO/Pt and GNP/Pt in 1 M H_2SO_4 solution at a scan rate of 20 mV s^{-1} between −0.2 V and 1.0 V vs SCE. (b) CVs of XC-72/Pt, RGO/Pt and GNP/Pt in 1 M H_2SO_4 and 2 M methanol solution at a scan rate of 20 mV s^{-1} between 0 V and 1.0 V vs SCE.

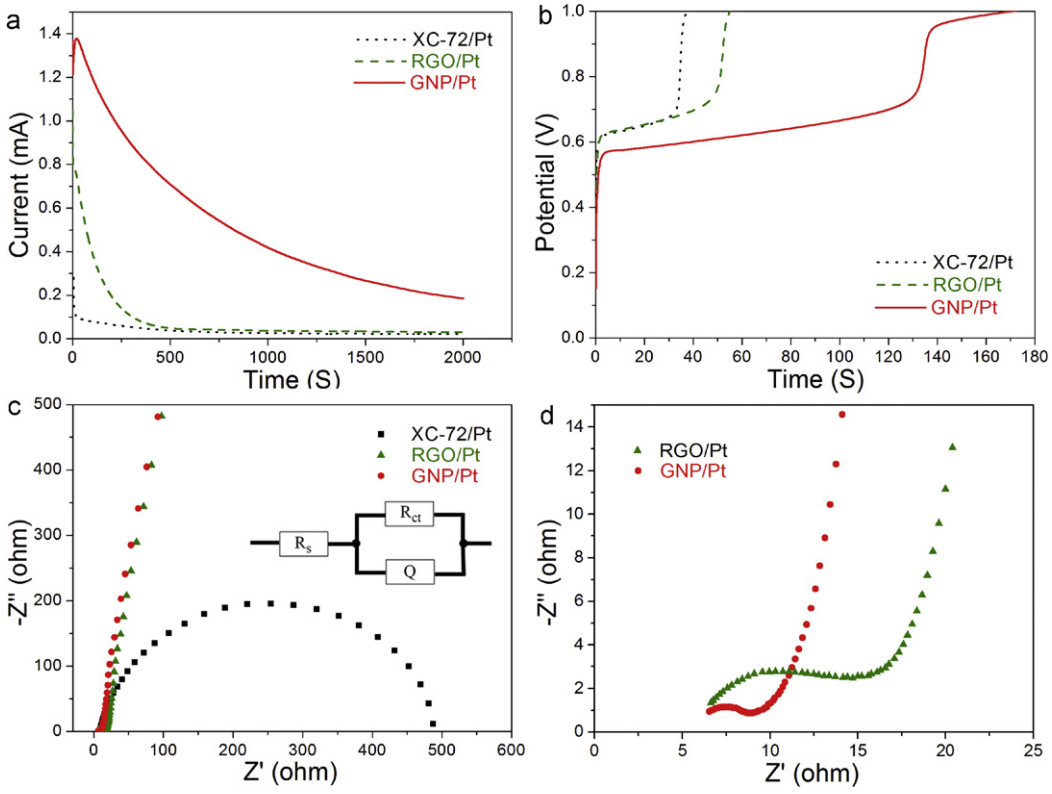

Fig. 6. (a) Chronoamperometric response recorded at 0.5 V (vs SCE) in 1 M H_2SO_4 and 2 M methanol solution for XC-72/Pt, RGO/Pt and GNP/Pt. (b) Chronopotentiometric curves of XC-72/Pt, RGO/Pt and GNP/Pt in 1 M H_2SO_4 and 2 M methanol solution. (c) Nyquist plots of EIS for XC-72/Pt, RGO/Pt and GNP/Pt at 0 V (vs SCE) in 1 M H_2SO_4 and 2 M methanol solution. The inset is the equivalent circuit used to fit the impedance spectra (d) Local enlargement of the Nyquist plots for RGO/Pt and GNP/Pt.

residual carbon species in the reverse scan. Fig. 5b clearly shows that the forward anodic peak current density for GNP/Pt composite is considerably higher than that of RGO/Pt, which is in good agreement with the result of ECSA. Moreover, the electrocatalytic activity of the RGO/Pt sample obtained by reduction of $Pt(NO_3)_2$ is similar to that of the sample obtained by reduction of K_2PtCl_4, as shown in Fig. S2. The ratio of the forward anodic peak current (I_F) to the reverse anodic peak current (I_R) can be used to describe the catalyst tolerance to the intermediate carbonaceous species accumulated on electrode surface [50]. A higher ratio indicates more effective removal of the poisoning species on the catalyst surface [16]. As can be seen from Table 1, the I_F/I_R ratio for GNP/Pt is found to be 1.4 times higher than that for RGO/Pt, implying that GNP/Pt has less carbonaceous accumulation and hence is much more tolerant toward CO poisoning. Meanwhile, compared with the composite of Vulcan XC-72, GNP shows higher electrocatalytic activity toward methanol oxidation and hence is a promising candidate material for fuel cell applications (Table 1). These significant improvements in the electrocatalytic performance can be attributed to the almost intact graphene structure in GNP/Pt and the high dispersion of Pt nanoparticles on GNP.

Improving durability is one of the most important research areas for fuel cell technology. The long-term electrocatalytic activities and stabilities of XC-72/Pt, RGO/Pt and GNP/Pt were examined by chronoamperometry for methanol oxidation at 0.5 V. At a fixed potential, the intermediate carbonaceous species such as CO would begin to accumulate on the electrode surface because of the continuous oxidation of methanol, which may poison the catalysts and decrease the performance [52]. As shown in Fig. 6a, all electrodes displayed an initial fast current decay followed by a slower attenuation upon long-time operation, gradually reaching a pseudo-steady state. The low stability of RGO/Pt can be ascribed to the following two reasons: one is that the conglomeration of Pt nanoparticles results in some of Pt particles cannot directly anchored to RGO support, and thereby suffers from more intermediate carbonaceous species accumulation [29]; and another is that the larger number of defect sites in the RGO were much easier to be corroded under harsh electrochemical conditions [37]. Among all the catalysts in this study, GNP/Pt was able to maintain the highest current density in the whole time, giving the best electrocatalytic performance. This result was attributed to the good preservation of the intrinsically electronic structure of graphene sheets in the composite and the high dispersion of Pt nanoparticles. Moreover, even when the outmost graphene layer is corroded, GNP with more graphene layers can retain its base graphitic structure [38].

Chronopotentiometry is a useful approach to study the antipoisoning abilities of catalysts for methanol oxidation. Fig. 6b shows the chronopotentiometric curves of XC-72/Pt, RGO/Pt and GNP/Pt catalysts, respectively. To diminish the influence of electrocatalytic activity of catalysts to the utmost extent, the value of the applied anodic current density is the same as that of the current density at 0.5 V on the forward branch of the corresponding cyclic voltammogram. As displayed in Fig. 6b, the electrode potential increases gradually at first and then instantaneously reaches to a much higher potential for all catalysts. The time at which the electrode potential jumps to a higher potential can be used to judge the antipoisoning ability of catalysts [53]. It is clearly seen that the sustained time for these catalysts decreases in the order GNP/Pt (~130 s) > RGO/Pt (~50 s) > XC-72/Pt (~30 s). In addition, the potential level of GNP/Pt is the lowest among these catalysts before the potential jumps. These results provide further evidence that GNP/Pt has the best electrocatalytic property and antipoisoning ability among the three catalysts.

Fig. 6c and d presents the Nyquist plots of EIS for XC-72/Pt, RGO/Pt and GNP/Pt obtained in 1 M H_2SO_4 and 2 M methanol solution at 0 V. The EIS plots of all samples contain a partially overlapped

Table 2
Impedance components for XC-72/Pt, RGO/Pt and GNP/Pt electrodes by fitting the experimental data using ZsimpWin software based on the equivalent circuit presented in the inset of Fig. 6c.

Electrode	R_{ct}	
	Value (ohm)	Error (%)
XC-72/Pt	473.5	3.8
RGO/Pt	15.0	5.0
GNP/Pt	4.5	3.9

semicircle. The charge transfer resistance in different catalysts can be estimated from the analysis of EIS spectra by using the software ZsimpWin based on an equivalent electric circuit as shown in the inset of Fig. 6c, where the R_s represents the uncompensated solution resistance, R_{ct} is charge transfer resistance of the catalyst and Q is a constant phase element [18,54]. The values for the parameters R_{ct} and their associated standard errors are summarized in Table 2. Obviously, the charge transfer resistances in graphene based composites are much lower than that in XC-72/Pt, implying graphene is a more appropriate electrocatalyst support for direct methanol fuel cells. In addition, it is clearly seen from Table 2 and Fig. 6d that GNP/Pt shows a remarkably lower R_{ct} value (4.5 Ω) than RGO/Pt (15.0 Ω), which can be contributed to the much lower defect density in GNP/Pt than that in RGO/Pt. The lower charge transfer resistance for the catalyst has good correlation with the higher electrocatalytic activity for methanol oxidation, suggesting that the GNPs supported electrocatalysts prepared by our method may be more competitive.

4. Conclusions

In summary, we have demonstrated a facile and controllable approach to synthesize GNP/Pt composite for DMFCs. TEM observations show that Pt nanoparticles were uniformly dispersed on graphene nanoplates. Raman analyzes provide evidence that only a very small amount of defects were introduced to the nanoplates by our approach. It has been found that GNP/Pt has better electrocatalytic activity and stability than RGO/Pt and XC-72/Pt for methanol oxidation, because the almost intact graphene structure in GNP/Pt hybrid significantly enhances the electrocatalytic activity of Pt nanoparticles and plays a key role in decreasing catalyst poisoning. This work could provide new insights into the fabrication of graphene nanoplate-Pt composites and facilitate their application in fuel-cell technologies.

Acknowledgements

The authors are grateful for the financial support of the Natural Science Foundation of China (No. 50902070), the National High Technology Research and Development Program of China (863 Program, No. 2010AA0500293002), a Project Funded by the Priority Academic Program Development of Jiangsu Higher Education Institutions, NUST Research Funding (2011PYXM03), and the Department of Education of Jiangsu Province (CXZZ11_0247).

Appendix A. Supplementary data

Supplementary data associated with this article can be found, in the online version, at doi:10.1016/j.jpowsour.2012.01.023.

References

[1] K. Sundmacher, Ind. Eng. Chem. Res. 49 (2010) 10159–10182.
[2] M. Winter, R.J. Brodd, Chem. Rev. 105 (2005) 1021.
[3] Y. Qiao, C.M. Li, J. Mater. Chem. 21 (2011) 4027–4036.
[4] A.S. Aricò, S. Srinivasan, V. Antonucci, Fuel Cells 1 (2001) 133–161.
[5] S. Basri, S.K. Kamarudin, W.R.W. Daud, Z. Yaakub, Int. J. Hydrogen Energy 35 (2010) 7957–7970.
[6] K.Y. Chan, J. Ding, J.W. Ren, S.A. Cheng, K.Y. Tsang, J. Mater. Chem. 14 (2004) 505–516.
[7] A. Halder, S. Sharma, M.S. Hegde, N. Ravishankar, J. Phys. Chem. C 113 (2009) 1466–1473.
[8] S.J. Guo, S.J. Dong, E.K. Wang, Adv. Mater. 22 (2010) 1269–1272.
[9] M. Carmo, A.R. Dos Santos, J.G.R. Poco, M. Linardi, J. Power Sources 173 (2007) 860–866.
[10] H.B. Zhao, L. Li, J. Yang, Y.M. Zhang, H. Li, Electrochem. Commun. 10 (2008) 876–879.
[11] J.H. Zeng, J.Y. Lee, W.J. Zhou, J. Power Sources 159 (2006) 509–513.
[12] C.A. Bessel, K. Laubernds, N.M. Rodriguez, R.T.K. Baker, J. Phys. Chem. B 105 (2001) 1115–1118.
[13] E.S. Steigerwalt, G.A. Deluga, C.M. Lukehart, J. Phys. Chem. B 106 (2002) 760–766.
[14] Y.L. Hsin, K.C. Hwang, C.T. Yeh, J. Am. Chem. Soc. 129 (2007) 9999–10010.
[15] H. Huang, D. Sun, X. Wang, J. Phys. Chem. C 115 (2011) 19405–19412.
[16] Y.Y. Mu, H.P. Liang, J.S. Hu, L. Jiang, L.J. Wan, J. Phys. Chem. B 109 (2005) 22212–22216.
[17] W.Z. Li, C.H. Liang, W.J. Zhou, J.S. Qiu, H.Q. Li, G.Q. Sun, Q. Xin, Carbon 42 (2004) 436–439.
[18] Y.H. Lin, X.L. Cui, C.H. Yen, C.M. Wai, Langmuir 21 (2005) 11474–11479.
[19] G. Girishkumar, K. Vinodgopal, P.V. Kamat, J. Phys. Chem. B 108 (2004) 19960–19966.
[20] G. Girishkumar, T.D. Hall, K. Vinodgopal, P.V. Kamat, J. Phys. Chem. B 110 (2006) 107–114.
[21] K.S. Novoselov, A.K. Geim, S.V. Morozov, D. Jiang, Y. Zhang, S.V. Dubonos, I.V. Grigorieva, A.A. Firsov, Science 306 (2004) 666–669.
[22] A.K. Geim, K.S. Novoselov, Nat. Mater. 6 (2007) 183–191.
[23] D. Li, M.B. Mueller, S. Gilje, R.B. Kaner, G.G. Wallace, Nat. Nanotechnol. 3 (2008) 101–105.
[24] S. Stankovich, D.A. Dikin, G.H.B. Dommett, K.M. Kohlhaas, E.J. Zimney, E.A. Stach, R.D. Piner, S.T. Nguyen, R.S. Ruoff, Nature 442 (2006) 282–286.
[25] C. Xu, X. Wang, J.W. Zhu, J. Phys. Chem. C 112 (2008) 19841–19845.
[26] R. Muszynski, B. Seger, P.V. Kamat, J. Phys. Chem. C 112 (2008) 5263–5266.
[27] Y.J. Li, W. Gao, L.J. Ci, C.M. Wang, P.M. Ajayan, Carbon 48 (2010) 1124–1130.
[28] L.F. Dong, R.R.S. Gari, Z. Li, M.M. Craig, S.F. Hou, Carbon 48 (2010) 781–787.
[29] S. Sharma, A. Ganguly, P. Papakonstantinou, X.P. Miao, M.X. Li, J.L. Hutchison, M. Delichatsios, S. Ukleja, J. Phys. Chem. C 114 (2010) 19459–19466.
[30] Y.M. Li, L.H. Tang, J.H. Li, Electrochem. Commun. 11 (2009) 846–849.
[31] C. Nethravathi, E.A. Anumol, M. Rajamathi, N. Ravishankar, Nanoscale 3 (2011) 569–571.
[32] S.M. Choi, M.H. Seo, H.J. Kim, W.B. Kim, Carbon 49 (2011) 904–909.
[33] S. Stankovich, D.A. Dikin, R.D. Piner, K.A. Kohlhaas, A. Kleinhammes, Y. Jia, Y. Wu, S.T. Nguyen, R.S. Ruoff, Carbon 45 (2007) 1558–1565.
[34] Y. Hernandez, V. Nicolosi, M. Lotya, F.M. Blighe, Z.Y. Sun, S. De, I.T. McGovern, B. Holland, M. Byrne, Y.K. Gun'ko, J.J. Boland, P. Niraj, G. Duesberg, S. Krishnamurthy, R. Goodhue, J. Hutchison, V. Scardaci, A.C. Ferrari, J.N. Coleman, Nat. Nanotechnol. 3 (2008) 563–568.
[35] G. Eda, G. Fanchini, M. Chhowalla, Nat. Nanotechnol. 3 (2008) 270–274.
[36] H.C. Schniepp, J.-L. Li, M.J. McAllister, H. Sai, M. Herrera-Alonso, D.H. Adamson, R.K. Prud'homme, R. Car, D.A. Saville, I.A. Aksay, J. Phys. Chem. B 110 (2006) 8535–8539.
[37] A. Barinov, O.B. Malciog lu, S. Fabris, T. Sun, L. Gregoratti, M. Dalmiglio, M. Kiskinova, J. Phys. Chem. C 113 (2009) 9009–9013.
[38] Y.Y. Shao, S. Zhang, C.M. Wang, Z.M. Nie, J. Liu, Y. Wang, Y.H. Lin, J. Power Sources 195 (2010) 4600–4605.
[39] S. Chen, J.W. Zhu, X. Wang, J. Solid State Chem. 184 (2011) 1393–1399.
[40] N.I. Kovtyukhova, P.J. Ollivier, B.R. Martin, T.E. Mallouk, S.A. Chizhik, E.V. Buzaneva, A.D. Gorchinskiy, Chem. Mater. 11 (1999) 771–778.
[41] W. Li, W. Zhou, H. Li, Z. Zhou, B. Zhou, G. Sun, Q. Xin, Electrochim. Acta 49 (2004) 1045–1055.
[42] S.F. Zheng, J.S. Hu, L.S. Zhong, L.J. Wan, W.G. Song, J. Phys. Chem. C 111 (2007) 11174–11179.
[43] J.J. Wang, G.P. Yin, J. Zhang, Z.B. Wang, Y.Z. Gao, Electrochim. Acta 52 (2007) 7042–7050.
[44] W.F. Chen, J.P. Wang, C.-H. Hsu, J.-Y. Jhan, H. Teng, P.-L. Kuo, J. Phys. Chem. C 114 (2010) 6976–6982.
[45] A.C. Ferrari, J. Robertson, Phys. Rev. B 61 (2000) 14095–14107.
[46] D. Graf, F. Molitor, K. Ensslin, C. Stampfer, A. Jungen, C. Hierold, L. Wirtz, Nano Lett. 7 (2007) 238–242.
[47] I. Calizo, A.A. Balandin, W. Bao, F. Miao, C.N. Lau, Nano Lett. 7 (2007) 2645–2649.
[48] A.C. Ferrari, J.C. Meyer, V. Scardaci, C. Casiraghi, M. Lazzeri, F. Mauri, S. Piscanec, D. Jiang, K.S. Novoselov, S. Roth, A.K. Geim, Phys. Rev. Lett. 97 (2006).
[49] A. Pozio, M. De Francesco, A. Cemmi, F. Cardellini, L. Giorgi, J. Power Sources 105 (2002) 13–19.
[50] R. Chetty, W. Xia, S. Kundu, M. Bron, T. Reinecke, W. Schuhmann, M. Muhler, Langmuir 25 (2009) 3853–3860.
[51] Y.C. Xin, J.G. Liu, Y. Zhou, W.M. Liu, J.A. Gao, Y. Xie, Y. Yin, Z.G. Zou, J. Power Sources 196 (2011) 1012–1018.
[52] B. Liu, J.H. Chen, C.H. Xiao, K.Z. Cui, L. Yang, H.L. Pang, Y.F. Kuang, Energy Fuels 21 (2007) 1365–1369.
[53] J.H. Chen, M.Y. Wang, B. Liu, Z. Fan, K.Z. Cui, Y. Kuang, J. Phys. Chem. B 110 (2006) 11775–11779.
[54] X.S. Peng, K. Koczkur, S. Nigro, A.C. Chen, Chem. Commun. (2004) 2872–2873.